Supplemental Material for
Equation of State of Liquid Iron under Extreme Conditions

Yasuhiro Kuwayama*, Guillaume Morard, Yoichi Nakajima*, Kei Hirose, Alfred Q. R. Baron, Saori I. Kawaguchi, Taku Tsuchiya, Daisuke Ishikawa, Naohisa Hirao, and Yasuo Ohishi

*Corresponding authors:
Yasuhiro Kuwayama, kuwayama@eps.s.u-tokyo.ac.jp
Yoichi Nakajima, yoichi@kumamoto-u.ac.jp

Contents:

1. High *P-T* XRD measurements

In-situ XRD measurements were conducted at the beamline BL10XU, SPring-8 synchrotron facility [9] (Table I). High *P-T* conditions were generated using LH-DAC techniques. We employed a symmetric DAC with flat 300 μm (run #1–9) or beveled 200 μm (run #10–11) culet diamond anvils, depending on a target pressure. Starting materials were pure iron foils (*Nilaco corp.*, 99.99%) with an initial thickness of 20 μm (run #1–9) or 15 μm (run #10–11). The sample was loaded into a hole at the center of a pre-indented rhenium gasket, together with thermal insulation layers of single-crystal Al_2O_3 sapphire. The single-crystal sapphire did not produce Debye rings in an XRD pattern, making data analyses easier.

To generate high *T* to melt iron and keep its molten state during XRD measurements, a single-crystal sapphire sleeve or Al_2O_3 powder was placed between the sample and the side wall of the gasket hole for better thermal insulation. We used KCl powder for a pressure medium instead of Al_2O_3 in runs #2 and #10 and obtained results consistent with those in the other runs. Both Al_2O_3 and KCl were found to be a good leak-proof container for liquid iron, which kept the molten sample at heating spot during collection of a diffuse scattering signal in XRD data. No chemical reaction was observed between these insulators and the iron sample from the microprobe analyses of recovered samples.

The sample assembly was dried in a vacuum oven at 423 K, at least for 6 hrs prior to pressurizing. Subsequently it was compressed to a target pressure at room temperature and then heated by a couple of 100 W single-mode Yb fiber lasers (*SPI Lasers Co. Ltd.*) from both sides. To reduce a radial temperature gradient, we employed beam shapers (*Newport Corp.*) that convert a beam with a Gaussian intensity distribution to the one with a flat-top distribution. The size of the laser-heated

spot was 40−50 μm across, which was much larger than the size of a focused incident x-ray beam (approximately 6 μm × 6 μm). The input powers of the two lasers were tuned so as to obtain temperature on both sides within less than 100 K differences.

Temperature was measured by a spectro-radiometric method. Thermal radiation spectra were collected every 0.3–1.0 sec with exposure time of 0.1–0.3 sec. Sample temperatures reported in this study are the average in 6 μm region, from which XRD data were collected, over entire XRD collection time (typically 1–2 sec). The temporal and spatial temperature variations in the 6 μm region were 70 K at 3000 K/40 GPa, and 300 K at 4300 K/116 GPa. The axial temperature gradient in the sample that was 5–10 μm thick at high pressures is estimated to be less than 100 K based on the thermal conductivity of liquid iron [36]. Thus, the total temperature uncertainty is estimated to be less than ±10 % (~170–400 K). The sample was heated only once in each run.

Angle-dispersive XRD patterns were collected sequentially during heating on a digital x-ray flat panel detector (*Perkin Elmer*, *XRD0822 CP23*, 1024 × 1024 pixels, 0.2 mm pixel pitch) with exposure time of 0.2 sec without interval. A series of five to ten two-dimensional XRD images were combined and integrated as a function of 2θ angle in order to produce a conventional one-dimensional diffraction pattern using the IP Analyzer program [37] (Fig. S1). The intense monochromatic incident x-ray beam with a wavelength of 0.04141(1)–0.04154(1) nm was focused on a sample by using stacked compound x-ray refractive lenses (CRLs), which enabled us to collect a diffuse signal from a liquid within short acquisition time.

Pressure at high T was determined by using the EoS for fcc iron in runs #1 and #3–8 [38] or hcp iron in runs #10–11 [29] from their lattice volumes observed just before complete melting (Table SI). Its error was derived from uncertainties in both temperature and the volume of iron. For runs #2 and #9, we could not determine the volume of fcc iron since only intense single-crystal-like diffraction spots, which exhibit blown-out highlights, were observed. Therefore, the pressures for these experiments were obtained from the unit-cell volume of the KCl pressure medium (Table SI) using its thermal EoS [39]. The advantage of the use of KCl is that uncertainty in temperature hardly affects the pressure calculated from its EoS because the thermal expansivity of KCl is very small [39]. The errors in pressure from KCl are estimated from uncertainties in its volume and the sample temperature.

After high P-T experiments, samples were recovered and polished parallel to the compression axis using a focused Ga ion beam (FIB) (*FEI*, *Versa3D DualBeam*). Chemical analyses were made for their cross sections with an energy-dispersive x-ray spectrometry (EDS) attached with a field-emission-type scanning electron microscope (FE-SEM) in the dual beam FIB system. Al, O, K, Cl, C and Re was not detected in quenched iron samples, indicating no chemical contamination by surrounding materials.

2. Density of liquid Fe from diffuse scattering signal

We determined the ρ of liquid iron from its in-situ XRD spectra by the following procedure (Table I). In order to obtain an x-ray scattering signal from a liquid sample I, subtraction of the background spectrum I_{bk} from the measured spectrum for a liquid I_{meas} is required. In this study, we measured I_{bk} just below the melting point of iron [30] and subsequently increased the sample temperature to 100–400 K above the melting temperature and collected I_{meas}. Since the intensity of incident x-ray beam fluctuated by approximately 2–5% during the collection of each XRD spectrum, the x-ray scattering signal from a liquid sample I is obtained by introducing a scale factor s as;

$$I(Q) = I_{\mathrm{meas}}(Q) - sI_{\mathrm{bk}}(Q), \tag{S1}$$

where $Q = 4\pi \sin\theta / \lambda$ is scattering momentum. It is normalized into atomic units and converted to structure factor $S(Q)$ as;

$$S(Q) = \alpha_{\mathrm{N}} \frac{I(Q)}{f_{\mathrm{Fe}}^2(Q)}, \tag{S2}$$

in which $f_{\mathrm{Fe}}(Q)$ is atomic form factor for iron [40] (different from $f(Q)$ in Eq. S3 below) and α_{N} is normalization factor. The $S(Q)$ of a monoatomic liquid is related to distribution function $F(r)$ and radial distribution function $g(r)$ by the following equations ("≡" represents definition);

$$f(Q) \equiv Q\{S(Q) - 1\}, \tag{S3}$$

$$F(r) \equiv 4\pi r\{\rho(r) - \rho\}, \tag{S4}$$

$$f(Q) = \int_0^\infty F(r) \sin(Qr)\, dr, \tag{S5}$$

$$F(r) = \frac{2}{\pi} \int_0^\infty f(Q) \sin(Qr)\, dQ\,, \tag{S6}$$

$$g(r) \equiv \frac{\rho(r)}{\rho} = 1 + \frac{F(r)}{4\pi r \rho}\,, \tag{S7}$$

where $\rho(r)$ is atomic density at a radial distance r (atoms per unit volume), and ρ is average atomic density. While Eq. S6 requires an integration to infinite Q, we can collect experimental data only in a limited range of Q. A termination of experimental data at finite Q generates artificial oscillations in calculated $F(r)$ and $g(r)$. Errors in s and α_{N} also yield large oscillations in $F(r)$ and $g(r)$ [41]. Although an iterative procedure has been widely used to eliminate these oscillations arising from the termination of data and the errors in s and α_{N} [11,13], such iterative procedure modifies $S(Q)$ from an experimentally observed profile, causing a partial loss of information from original data.

In this study, we have developed a new procedure, in which observed $S(Q)$ is extended beyond the experimental Q range so that the resultant $F(r)$ and $g(r)$ behave physically reasonable, instead of iterative procedures used in previous studies [11,13]. Here $S(Q)$ observed in the experimental Q range is never modified. Our new method described below is similar to the procedure for determination of $g(r)$ proposed by Kaplow *et al.* [41] but is better prescribed. We describe the source of artificial oscillations in $F(r)$ and $g(r)$ in section 2-1, how to extend the observed $S(Q)$ and $f(Q)$ in section 2-2, analytical procedures to determine ρ from experimental data in section 2-3, and validation of the present new analytical method in section 2-4.

2-1. The source of the oscillations in *F*(*r*) and *g*(*r*). In this section, we show that oscillations in $F(r)$ and $g(r)$ caused by the termination of experimental data at finite Q can be divided into two components.

If true $f(Q)$ (= $Q\{S(Q) - 1\}$, Eq. S3) is known for the full Q range (hereafter $f_\infty(Q)$), the equivalent true distribution function $F_\infty(r)$ and radial distribution function $g_\infty(r)$ can be calculated by Eqs. S6 and S7 (Fig. S3A). Since no atom exists within the distance between the nearest neighbor atoms (r_{min});

$$g(r) = 0 \ \ (r < r_{\mathrm{min}}), \tag{S8}$$

Eq. S7 yields;

$$F(r) = -4\pi\rho r \ \ (r < r_{\mathrm{min}}), \tag{S9}$$

indicating that true $F(r)$ at the $r < r_{\mathrm{min}}$ region is a linear equation of r. Density ρ can thus be obtained from true $F(r)$ at $r < r_{\mathrm{min}}$ (Eq. S9).

In our experiments, however, $f(Q)$ is truncated at a finite $Q_{\max}$. Hereafter $f_{Q\max}(Q)$ represents $f(Q)$ that is terminated at $Q_{\max}$ as;

$$f_{Q_{\max}}(Q) \equiv \begin{cases} f_{\infty}(Q) & (Q \le Q_{\max}) \\ 0 & (Q > Q_{\max}) \end{cases}, \tag{S10}$$

and $F_{Q\max}(r)$ and $g_{Q\max}(r)$ represent calculated $F(r)$ and $g(r)$ from $f_{Q\max}(Q)$ as;

$$F_{Q_{\max}}(r) \equiv \frac{2}{\pi}\int_0^{\infty} f_{Q_{\max}}(Q)\sin(Qr)\,dQ\,, \tag{S11}$$

$$g_{Q_{\max}}(r) \equiv\ 1 + \frac{F_{Q_{\max}}(r)}{4\pi r\rho}. \tag{S12}$$

As illustrated in Fig. S3B, the truncation of $f(Q)$ at $Q_{\max}$ leads to artificial oscillations in calculated $F_{Q\max}(r)$ and $g_{Q\max}(r)$.

In order to evaluate the effect of such truncation, we define $\Delta f(Q)$, $\Delta F(r)$, and $\Delta g(r)$ (Fig. S3C) as;

$$\Delta f(Q) \equiv f_{\infty}(Q) - f_{Q_{\max}}(Q), \tag{S13}$$

$$\Delta F(r) \equiv F_{\infty}(r) - F_{Q_{\max}}(r), \tag{S14}$$

$$\Delta g(r) \equiv g_{\infty}(r) - g_{Q_{\max}}(r). \tag{S15}$$

Note that $\Delta f(Q)$ is the Fourier transform of $\Delta F(r)$ as;

$$\Delta f(Q) = \int_0^{\infty} \Delta F(r)\sin(Qr)\,dr\,, \tag{S16}$$

$$\Delta F(r) = \frac{2}{\pi}\int_0^{\infty} \Delta f(Q)\sin(Qr)\,dQ, \tag{S17}$$

and $\Delta g(r)$ is;

$$\Delta g(r) = \frac{\Delta F(r)}{4\pi r\rho}. \tag{S18}$$

Next we divide $\Delta F(r)$ and $\Delta g(r)$ into those at $r < r_{\min}$ and $r \ge r_{\min}$ regions (Fig. S4) as;

$$\Delta F_1(r) \equiv \begin{cases} \Delta F(r) & (r < r_{\min}) \\ 0 & (r \ge r_{\min}) \end{cases}, \tag{S19}$$

$$\Delta F_2(r) \equiv \begin{cases} 0 & (r < r_{\min}) \\ \Delta F(r) & (r \ge r_{\min}) \end{cases}, \tag{S20}$$

$$\Delta g_1(r) \equiv \begin{cases} \Delta g(r) & (r < r_{\min}) \\ 0 & (r \ge r_{\min}) \end{cases}, \tag{S21}$$

$$\Delta g_2(r) \equiv \begin{cases} 0 & (r < r_{\min}) \\ \Delta g(r) & (r \ge r_{\min}) \end{cases}. \tag{S22}$$

The Fourier transforms of $\Delta F_1(r)$ and $\Delta F_2(r)$ are $\Delta f_1(Q)$ and $\Delta f_2(Q)$, respectively (Fig. S4);

$$\Delta f_1(Q) \equiv \int_0^{\infty} \Delta F_1(r)\sin(Qr)\,dr\,, \tag{S23}$$

$$\Delta f_2(Q) \equiv \int_0^{\infty} \Delta F_2(r)\sin(Qr)\,dr\,. \tag{S24}$$

Note that

$$\Delta f_1(Q) + \Delta f_2(Q) = \Delta f(Q). \tag{S25}$$

Since $\Delta f(Q) = 0$ at $Q \leq Q_{\max}$ (Eq. S10, Fig. S3C), Eq. S25 indicates (Fig. S4);

$$\Delta f_1(Q) + \Delta f_2(Q) = 0 \quad (Q \leq Q_{\max}). \tag{S26}$$

We further divide $\Delta f_1(Q)$ and $\Delta f_2(Q)$ into those at $Q > Q_{\max}$ and $Q \leq Q_{\max}$ regions (Fig. S5) as;

$$\Delta f_{1A}(Q) \equiv \begin{cases} 0 & (Q \leq Q_{\max}) \\ \Delta f_1(Q) & (Q > Q_{\max}) \end{cases}, \tag{S27}$$

$$\Delta f_{1B}(Q) \equiv \begin{cases} \Delta f_1(Q) & (Q \leq Q_{\max}) \\ 0 & (Q > Q_{\max}) \end{cases}, \tag{S28}$$

$$\Delta f_{2A}(Q) \equiv \begin{cases} 0 & (Q \leq Q_{\max}) \\ \Delta f_2(Q) & (Q > Q_{\max}) \end{cases}, \tag{S29}$$

$$\Delta f_{2B}(Q) \equiv \begin{cases} \Delta f_2(Q) & (Q \leq Q_{\max}) \\ 0 & (Q > Q_{\max}) \end{cases}. \tag{S30}$$

Since $\Delta f_{1B}(Q) + \Delta f_{2B}(Q) = 0$ from Eqs. S26, S28, and S30, we find $\Delta f(Q) = \Delta f_{1A}(Q) + \Delta f_{2A}(Q)$, and thus $f_\infty(Q)$ can be expressed as;

$$f_\infty(Q) = f_{Q_{\max}}(Q) + \Delta f_{1A}(Q) + \Delta f_{2A}(Q). \tag{S31}$$

When we define $\Delta F_{1A}(r)$, $\Delta F_{2A}(r)$, $\Delta g_{1A}(r)$, and $\Delta g_{2A}(r)$ as;

$$\Delta F_{1A}(r) \equiv \frac{2}{\pi}\int_0^\infty \Delta f_{1A}(Q)\sin(Qr)\,dQ\,, \tag{S32}$$

$$\Delta F_{2A}(r) \equiv \frac{2}{\pi}\int_0^\infty \Delta f_{2A}(Q)\sin(Qr)\,dQ\,, \tag{S33}$$

$$\Delta g_{1A}(r) \equiv \frac{\Delta F_{1A}(r)}{4\pi r\rho}, \tag{S34}$$

$$\Delta g_{2A}(r) \equiv \frac{\Delta F_{2A}(r)}{4\pi r\rho}, \tag{S35}$$

$F_\infty(r)$ and $g_\infty(r)$ can also be expressed by three components (Fig. S6) as;

$$F_\infty(r) = F_{Q_{\max}}(r) + \Delta F_{1A}(r) + \Delta F_{2A}(r), \tag{S36}$$

$$g_\infty(r) = g_{Q_{\max}}(r) + \Delta g_{1A}(r) + \Delta g_{2A}(r). \tag{S37}$$

Note that $\Delta F_{1A}(r)$ is a Fourier transform of $\Delta f_{1A}(Q)$, which is $\Delta f_1(Q)$ at $Q > Q_{\max}$. The inverse Fourier transform of $\Delta f_1(Q)$ is $\Delta F_1(r)$, which corresponds to the difference between true $F_\infty(r) = -4\pi r\rho$ and $F_{Q\max}(r)$ at $r < r_{\min}$. $\Delta g_{1A}(r)$ is obtained from $\Delta F_{1A}(r)$ (Eq. S34). Thus, $\Delta F_{1A}(r)$ can be calculated from observed $f_{Q\max}(Q)$. On the other hand, we cannot estimate $\Delta F_{2A}(r)$ and $\Delta g_{2A}(r)$ because we do not have any constraints on $\Delta F(r)$ and $\Delta g(r)$ at $r \geq r_{\min}$ (= $\Delta F_2(r)$ and $\Delta g_2(r)$), but $\Delta F_{2A}(r)$ and $\Delta g_{2A}(r)$ contribute little to $\Delta F(r)$ and $\Delta g(r)$ as shown later (Fig. S6). In summary, the oscillations in $F(r)$ and $g(r)$ can be described by the two components, $\Delta F_{1A}(r)$ and $\Delta F_{2A}(r)$. $\Delta F_{1A}(r)$ is a main source of the oscillations and can be calculated from experimental data. Using these relations, we consider the extension of $f(Q)$ in order to reduce artificial oscillations in calculated $F(r)$ and $g(r)$ in the following section.

2-2. Extension of $f(Q)$ beyond experimental limit Q_{max}. If true ρ and r_{min} are given, $\Delta f_{1A}(Q)$ (Eq. S27) can be calculated using the physical requirement $F_\infty(r) = -4\pi\rho r$ (or $g_\infty(r) = 0$) at $r < r_{min}$ (while we cannot estimate $\Delta f_{2A}(Q)$ as mentioned in Sec. 2-1). Now, we consider the extension of $f(Q)$ (Fig. S7) beyond experimental limit Q_{max} using $\Delta f_{1A}(Q)$ as;

$$f_{\mathrm{extend}}(Q) \equiv f_{Q_{\mathrm{max}}}(Q) + \Delta f_{1A}(Q). \tag{S38}$$

From Eqs. S31, S32, S34, S36 and S37, we find that;

$$\begin{aligned} F_{\mathrm{extend}}(r) &\equiv F_{Q_{\mathrm{max}}}(r) + \Delta F_{1A}(r) \\ &= F_\infty(r) - \Delta F_{2A}(r), \end{aligned} \tag{S39}$$

$$\begin{aligned} g_{\mathrm{extend}}(r) &\equiv g_{Q_{\mathrm{max}}}(r) + \Delta g_{1A}(r) \\ &= g_\infty(r) - \Delta g_{2A}(r), \end{aligned} \tag{S40}$$

in which $F_{extend}(r)$ and $g_{extend}(r)$ represent calculated $F(r)$ and $g(r)$ from $f_{extend}(Q)$ (Fig. S7B and S7C). Eqs. S39 and S40 indicate that $F_{extend}(r)$ and $g_{extend}(r)$ still include artificial oscillations of $-\Delta F_{2A}(r)$ and $-\Delta g_{2A}(r)$, respectively. However, the contribution of $\Delta F_{1A}(r)$ to $\Delta F(r)$ is much more than that of $\Delta F_{2A}(r)$ at $r < r_{min}$ (Figs. S6A and S6B). Therefore, the artificial oscillation in $F_{extend}(r)$ (or $g_{extend}(r)$) is reduced largely when compared to that in $F_{Qmax}(r)$ (Fig. S7B) (or $g_{Qmax}(r)$, Fig. S7C).

2-3. Analyses of experimental data. Next, let's look at experimental data obtained in this study. An experimental $f(Q)$, $f_{obs}(Q)$, is obtained from raw data using background scale factor s and normalization factor α_N (Eqs. S1 and S2). When both s and α_N are correct, $f_{obs}(Q)$ truncated at finite Q_{max} is equal to $f_{Qmax}(Q)$ (= true $f_\infty(Q)$ at $Q \le Q_{max}$). $F_{Qmax}(r)$ and $g_{Qmax}(r)$ are calculated from observed $f_{obs}(Q)$ (= $f_{Qmax}(Q)$) using Eqs. S11 and S12. If true ρ and r_{min} are known, true $F_\infty(r)$ at $r < r_{min}$ should be $-4\pi\rho r$ (Fig. S3A) and thus $\Delta F_1(r)$ (Eq. S19) is;

$$\Delta F_1(r) = \begin{cases} -4\pi\rho r - F_{Q_{\mathrm{max}}}(r) & (r < r_{\mathrm{min}}) \\ 0 & (r \ge r_{\mathrm{min}}) \end{cases}. \tag{S41}$$

Using Eqs. S11, S23, S27, S38, and S41, we can extend the observed $S(Q)$ (and $f(Q)$) beyond the experimental Q range as described in Eq. 1 in the main text.

In practice, however, ρ is not known. So we first employ an input ρ which generally includes errors $\Delta\rho$ as $\rho_{input} = \rho_{true} + \Delta\rho$. For ρ_{input}, the calculated $\Delta F_1(r)$ is;

$$\Delta F_1(r) = \begin{cases} -4\pi(\rho_{\mathrm{true}} + \Delta\rho)r - F_{Q_{\mathrm{max}}}(r) & (r < r_{\mathrm{min}}) \\ 0 & (r \ge r_{\mathrm{min}}) \end{cases}. \tag{S42}$$

When $f_{obs}(Q)$ (= $f_{Qmax}(Q)$) is extended to $f_{extend}(Q)$ using $\Delta f_{1A}(Q)$ that is calculated from $\Delta F_1(r)$, $F_{extend}(r)$ obtained from $f_{extend}(Q)$ includes additional terms arising from $-4\pi\Delta\rho r$ in $\Delta F_1(r)$, as given by Eq. 2 in the main text, compared to those calculated for true ρ. Thus, the input ρ is correct (in other word, $\Delta\rho = 0$), when the difference between the calculated $F_{extend}(r)$ matches the expected $F(r)$ $= -4\pi\rho r$ (or the calculated $g_{extend}(r) = 0$) at $r < r_{min}$. The density of liquid, ρ, is obtained in this manner. Similarly, the true r_{min} value, that defines the range where true $F_\infty(r) = -4\pi\rho r$, is also unknown. When assumed r_{min} is smaller than the true r_{min}, $f_{extend}(Q)$ is less complemented, resulting in larger oscillations in $F_{extend}(r)$ and $g_{extend}(r)$. A large r_{min} also gives inappropriate $f_{extend}(Q)$ leading to larger oscillations. We therefore need to search for r_{min} for such oscillations to be the smallest.

Furthermore, both s and α_N used to calculate $f_{obs}(Q)$ (Eqs. S1 and S2) are also not known. When these values are not correct, $f_{obs}(Q)$ is not equal to $f_{Qmax}(Q)$, and $\Delta f(Q)$ = true $f_\infty(Q) - f_{obs}(Q)$ is not zero even at $Q \le Q_{max}$, which causes further additional terms and thus oscillations in $F_{extend}(r)$ and $g_{extend}(r)$ (Fig. S8). Therefore, we search also for s and α_N for such oscillations to be the smallest.

To summarize, when true s, α_N, ρ and r_{min} are found, the calculated $g_{extend}(r)$ is close to zero at $r < r_{min}$, which is physically expected (Fig. 1(b)).

In this study, we have sought for the best $f_{extend}(Q)$, as well as s, α_N, ρ, and r_{min}, which makes $g_{extend}(r) \cong 0$ at $r < r_{min}$, minimizing a figure of merit χ^2 that is given by:

$$\chi^2(s, \alpha_N, \rho, r_{min}) \equiv \int_0^{r_{min}} \{g_{extend}(r)\}^2 dr\,, \tag{S43}$$

similar in a previous study [11]. The difference between the present method and the one in previous study [11] is that we calculate $g_{extend}(r)$ from extended $S_{extend}(Q)$, in which $S(Q)$ for $Q \leq Q_{max}$ is not modified from experimental data, while the earlier study [11] calculated $g(r)$ from $S(Q)$ that was modified by iterative procedure, potentially losing information from raw data.

In practice, the magnitude and shape of the oscillation in $F_{extend}(r)$ and $g_{extend}(r)$ are also affected by Q_{max} in Eq. 1 [16,17]. This is because residual oscillations in $F_{extend}(r)$ and $g_{extend}(r)$ are equal to $-\Delta F_{2A}(r)$ and $-\Delta g_{2A}(r)$, respectively. Such $-\Delta F_{2A}(r)$ and $-\Delta g_{2A}(r)$ vary with Q_{max} since, for example, Q_{max} defines $f_{Qmax}(Q)$ from which $F_{Qmax}(r)$ and $\Delta F(r)$ are obtained. Therefore, we look for the minimum χ^2 with changing Q_{max} in Eq. 1 from the experimental limit to ~30 nm^{-1} (corresponding to the end of the first dominant peak in $S(Q)$ at 30−35 nm^{-1}). The calculation shows that there is a unique value of Q_{max} which minimizes χ^2 for each experimental data.

Fig. S9 shows contour plots for χ^2 in the α_N–ρ and s–ρ space for run #1. In Fig. S9A, each χ^2 is the minimum value for a given set of (α_N, ρ) values, which is found by changing s, Q_{max}, and r_{min}. This is illustrated in a different way in Fig. S9C; each panel corresponds to a specific pair of (α_N, ρ) and shows χ^2 as a function of s with simultaneously changing Q_{max} and r_{min}. Similarly in Fig. S9B, the minimum χ^2 was searched for a specific set of (s, ρ) values by varying α_N, Q_{max}, and r_{min}. We found a unique set of parameters that minimizes χ^2; s = 1.0052, Q_{max} = 72.0, r_{min} = 0.194, α_N = 4.522, and ρ = 85.26 atoms/nm^3 (7.91 g/cm^3), giving us the density of liquid iron at 22 GPa and 2600 K. The structure factor $S(Q)$ for run #1 with these parameters and the corresponding $g_{extend}(r)$ are shown in Fig. 1. $g_{extended}(r) \cong 0$ at $r < r_{min}$ is physically reasonable. The uncertainty in ρ is estimated from the difference between calculated $F_{extend}(r)$ and expected $F(r) = -4\pi\rho r$. The calculated standard error in ρ from $F_{extend}(r)$ is 0.73 atoms/nm^3 (0.86 %) (Table I). The errors are less than ~1.5% for all runs.

While we neglected the high-frequency noises in the observed spectra (Fig. S1), it hardly affects density determinations, since the effect of the high-frequency component in $S(Q)$ on calculated $g(r)$ at $r < r_{min}$ is limited.

2-4. Validation of the present new analytical method. We have verified our new method by analyzing 1) the XRD data previously collected for a Ce-based metallic glass ($Ce_{70}Al_{10}Ni_{10}Cu_{10}$) and 2) a synthetic XRD pattern.

1) We employed the XRD data for a metallic glass $Ce_{70}Al_{10}Ni_{10}Cu_{10}$ collected near ambient condition (<0.5 GPa and 300 K) (Fig. S10A) [42]. Since the background signal of this data was obtained by measuring a DAC containing only He pressure medium without sample, we need to subtract incoherent (Compton) scattering from the measured spectrum. Therefore, Eq. S1 is rewritten as;

$$I(Q) = I_{meas}(Q) - \frac{\sum I_{incoh}(Q)}{\alpha_N} - sI_{bk}(Q), \tag{S44}$$

where $\sum I_{incoh}(Q)$ is the sum of the incoherent scattering signals [40] from a sample. In addition, instead of Eq. S2, the structure factor $S(Q)$ for polyatomic compounds, such as the Ce-based metallic glass, is written as;

$$S(Q) = \frac{\{\alpha_N I(Q) - (\langle f^2 \rangle - \langle f \rangle^2)\}}{\langle f \rangle^2}, \quad \text{(S45)}$$

where $\langle f^2 \rangle$ and $\langle f \rangle^2$ are defined as;

$$\langle f^2 \rangle = \sum_i X_i f_i^2(Q), \quad \text{(S46)}$$

$$\langle f \rangle^2 = \sum_i \sum_j X_i f_i(Q) X_j f_j(Q), \quad \text{(S47)}$$

in which X_i and $f_i(Q)$, for example, are the fraction and atomic form factor [40] of atomic specie i in the sample (see [42] for more details). Using Eqs. S44–S47, the new analytical method described above was applied to the Ce-based glass data. As illustrated in Figs. S10B and S10C, the resultant $F_{extend}(r)$ and $g_{extend}(r)$ were calculated from the extended structure factor $S_{extend}(Q)$ with parameters which minimize χ^2. The atomic density is found to be 36.5 ± 0.2 atoms/nm^3. It is in good agreement with that reported in previous study (36.4 ± 2.0 atoms/nm^3) [42]. More importantly, the uncertainty is much smaller. This value is slightly larger than that determined at ambient condition by Archimedean technique (35.6 atoms/nm^3) [43], because the XRD data employed here was collected under a modest pressure between 0.2 and 0.5 GPa to keep He pressure medium in a sample chamber.

2) In order to show our new method is universally valid, we also analyzed a synthetic XRD pattern. We first made in a random manner synthetic model distribution function $F_{model}(r)$ and radial distribution function $g_{model}(r)$ of a non-crystalline material with ρ = 74.4 atoms/nm^3 (Fig. S11A). The $F_{model}(r)$ is converted to $f_{model}(Q)$ and model structure factor $S_{model}(Q)$ (Fig. S11B). The $S_{model}(Q)$ is further converted to model diffuse scattering signal $I_{model}(Q)$, considering α_N = 5 (Fig. S11C). Since measurements always include a background signal, we also prepared a model background signal $I_{bk\_model}(Q)$ (Fig. S11D). A model XRD spectrum $I_{meas\_model}(Q)$ was then obtained by adding $I_{bk\_model}(Q)$ to $I_{model}(Q)$ using a scale factor s = 0.9 (Fig. S11E). The observable Q range is practically limited to about 70–120 nm^{-1} in a high-pressure apparatus. Therefore, the model $I_{meas\_model}(Q)$ and $I_{bk\_model}(Q)$ are terminated at Q_{max} = 85 nm^{-1} (Fig. S11F) (hereafter, $I_{meas\_Q85}(Q)$ and $I_{bk\_Q85}(Q)$ represent $I_{meas\_model}(Q)$ and $I_{bk\_model}(Q)$ that are terminated at Q = 85 nm^{-1}). These ρ, α_N, s, and Q_{max} values do not refer to specific materials and conditions.

We then tried to reproduce ρ = 74.4 atoms/nm^3 from $I_{meas\_Q85}(Q)$ and $I_{bk\_Q85}(Q)$ using our new method. $F_{Qmax}(r)$ and $g_{Qmax}(r)$ directly calculated from the $I_{meas\_Q85}(Q)$ and $I_{bk\_Q85}(Q)$ include large oscillations particularly at a small r region (blue profiles in Fig. S12), mainly because of the termination of data at Q = 85 nm^{-1} and uncertain parameters such as s and α_N. Nevertheless, the present new method provided $F_{extend}(r)$ and $g_{extend}(r)$ (red profiles in Fig. S12) from the extended structure factor $S_{extend}(Q)$ with parameters that minimize χ^2, in which the oscillations were reduced to a large extent at the small r region. We found ρ = 74.2 atoms/nm^3 with s = 0.9014 and α_N = 5.006, which differs from the model density only by 0.2 atoms/nm^3 (0.3%). The calculated standard error in ρ from $F_{extend}(r)$ is 0.4 atoms/nm^3 (0.5%), indicating that the new method well reproduces the initial model $F(r)$ at a small r region.

In contrast to our new analytical method, previous studies have used an iterative analytical procedure [11] to determine densities of amorphous materials. However, the iterative procedure modifies measured $S(Q)$ to reduce oscillations in $F(r)$, causing the loss of information from raw measured data. As a result, the procedure sometimes works when the modification is not significant [12,13], but it sometimes fails [4,16]. The most serious problem of such iterative method is that one cannot judge whether the procedure works or not, because there is no way to quantitatively evaluate how much the modification of $S(Q)$ during the iterative procedure changes a density value obtained. In this study, the present new analytical method has overcome this problem and successfully removes the oscillation in $F(r)$ at a small r region by quantitatively extending $S(Q)$ using Eq. 1 in the main text. In contrast to the iterative procedure, our new method does not modify measured

$S(Q)$, not causing the loss of information from raw data. As we described here, our new analytical method is universally applicable for density determinations of amorphous materials.

3. Inelastic x-ray scattering measurements

Inelastic x-ray scattering (IXS) spectra were collected at the RIKEN Quantum NanoDynamics Beamline, BL43XU [21,44] of SPring-8 (Table I). High *P-T* conditions were generated by LH-DAC techniques, similar to the XRD experiments described above. Flat 300 μm culet diamond anvils were used. Iron foil with 15−20 μm thickness (*Nilaco corp.*, 99.99%) was used as a starting material. It was loaded into a hole in a rhenium gasket, together with 15–20 μm thick single-crystal Al_2O_3 sapphire discs that served as both thermal and chemical insulators. The sample assembly was dried in a vacuum oven at 423 K for at least 6 hrs and then compressed to a pressure of interest at room temperature. The sample was heated to a temperature comparable to or higher than the melting temperature of iron [30] using a couple of 200 W single-mode Yb^{2+}-doped fiber lasers (*YLR-200*, *IPG Photonics Corp.*). In order to minimize the radial temperature gradient, a laser beam had a flat-top intensity distribution after passing through a beam shaper (*GBS-NIR-H3*, *Newport Corp.*). A laser heated spot size was 40–60 μm in diameter, much larger than the x-ray beam size of 5–12 μm (FWHM). Temperature was measured by a spectro-radiometric method, and its temporal and spatial variations within the area irradiated by x-rays during IXS measurements were less than ±10 %. During laser heating, the XRD patterns of the sample were monitored using a 2D flat panel detector (*C9732DK, Hamamatsu Photonics K.K.*) installed at the beamline. Pressure was determined from the lattice volume of fcc iron observed just before melting [38]. Its error was derived from uncertainties in both temperature and the volume of iron.

The sound velocity of liquid iron in a DAC was determined by high-resolution IXS spectroscopy [20] (Table I). A DAC was placed into a vacuum chamber to minimize the background scattering by air. Before and after collecting the IXS data, the molten state of an iron sample was carefully confirmed by the absence of its diffraction peaks (Fig. S13). We sometimes observed, depending on a sample volume, a diffuse scattering signal from liquid. The IXS measurements were carried out with ~2.8 meV energy resolution using Si (999) backscattering geometry at 17.79 keV. Experimental energy resolutions were obtained using the scattering from polymethyl-methacrylate (PMMA). The incident x-ray beam was focused to about 12 μm × 10 μm (FWHM) using compound focusing, or 5 μm × 5 μm using a Kirkpatrick–Baez mirror system [21]. Scattered photons were collected at momentum transfers (Q) between 3.0–5.7 nm^{-1} with a resolution of ΔQ ~ 0.4–0.6 nm^{-1} (full width) that was set by slits in front of the analyzer array. A typical energy transfer range of ±20 meV was scanned for about 30 min.

The IXS spectra include several components in the present scanned energy range (Fig. 3(a)); Stokes and anti-Stokes components of the longitudinal acoustic (LA) phonon mode from the sample and of the transverse acoustic (TA) mode form the diamond anvils, and a quasi-elastic contribution near zero energy transfer. The spectra were fitted with the damped harmonic oscillator (DHO) mode [45] for acoustic phonon modes and with a Lorentzian function for quasi-elastic peaks convolved by experimental resolution function. The DHO model function can be described as:

$$S^{\mathrm{DHO}}(Q,\omega) = \left[\frac{1}{1-e^{-\hbar\omega/k_{\mathrm{B}}T}}\right]\frac{A_{\mathrm{Q}}}{\pi}\frac{4\omega\omega_Q\gamma_Q}{\left(\omega^2-{\Omega_Q}^2\right)^2+4{\gamma_Q}^2\omega^2}, \tag{S48}$$

where A_Q, Γ_Q, ω_Q, k_{B}, and $\hbar$ are the amplitude, width, and energy of inelastic modes, Boltzmann constant, and Planck constant, respectively. Temperature T is a sample temperature obtained by a spectroradiometric method. The peak at a finite energy transfer gives the frequency of each mode.

The dispersion relation of the excitation energies ($E = \hbar\omega$) for the LA phonon mode as a function of Q was obtained at each pressure (Fig. 3(b)).

Compressional sound wave or P-wave velocity (V_P) corresponds to the long-wavelength LA velocity at $Q \rightarrow 0$ limits:

$$V_P = \left(\frac{dE}{dQ}\right)_{Q\rightarrow 0}. \tag{S49}$$

We fitted a linear function to the data obtained at the lowest Q = 3.0 nm^{-1} to determine the P-wave velocity (Table I) because positive dispersion possibly appears in liquids at the higher Q range [45]. The error in V_P was derived from uncertainty in the energy for the longitudinal acoustic phonon mode at Q = 3 nm^{-1}, which was found to be 0.4–0.6 meV (one standard deviation) based on the least squares fitting to raw IXS spectra. See our previous studies for further details [23,46].

4. EoS of liquid iron

We have obtained the Mie-Grüneisen EoS for liquid iron from its P-T-ρ data and the P-T-V_P data (Fig. 4);

$$P(x,T) = P_{T_0}(x) + \Delta P_{\mathrm{th}}(x,T), \tag{S50}$$

in which total pressure $P(x, T)$ is the sum of pressure at a reference temperature $P_{T_0}(x)$ and thermal pressure $\Delta P_{\mathrm{th}}(x,T)$ ($x = \rho_0 / \rho$, and ρ_0 is the density at zero pressure and a reference temperature T_0). In this study, T_0 is set to be 1811 K (melting point of iron at 1 bar). For the isothermal part at T_0, we used the Vinet (Morse-Rydberg) equation;

$$P_{T_0}(x) = 3K_{T_0}x^{-\frac{2}{3}}\left(1-x^{\frac{1}{3}}\right)\exp\left\{\frac{3}{2}\left(K'_{T_0}-1\right)\left(1-x^{\frac{1}{3}}\right)\right\}, \tag{S51}$$

where K_{T_0} and K'_{T_0} are isothermal bulk modulus and its pressure derivative at zero pressure and T_0, respectively. For the thermal pressure part, the quasi-harmonic Debye model has been widely used [29]. However, electronic effect is not negligible in metals particularly at high temperatures of the Earth's core [29,47]. A previous study [29] on the EoS of solid iron incorporated the anharmonic effect in addition to quasi-harmonic Debye thermal pressure, but such quasi-harmonic approximation is inadequate for liquids. Alternatively, since our data were collected only at temperatures much higher than the Debye temperature (the Duong-Petit limit), the Debye function approaches the constant value of 1/3, and the phonon energy can be expressed as a linear function of temperature. We therefore adopt a suite of EoS functions for metallic liquids recently proposed by Ichikawa *et al.* [47], assuming that internal thermal energy is simply represented by a second-order polynomial of temperature with a volume dependent second-order coefficient as;

$$E_{\mathrm{th}}(x,T) = 3nR(T + e_0 x^g T^2), \tag{S52}$$

where n is the number of atoms in formula unit, R is gas constant, and both e_0 and g are constants. The first term corresponds to atomic contribution, and the second term represents electronic one. Using the thermal energy $E_{\mathrm{th}}(x,T)$ and the Grüneisen parameter (γ), thermal pressure is expressed as;

$$\Delta P_{\mathrm{th}}(x,T) = \frac{\gamma(x)}{V}\Delta E_{\mathrm{th}}(x,T) = \frac{\gamma(x)}{V}[E_{th}(x,T) - E_{th}(x,T_0)]. \tag{S53}$$

The volume dependence of γ is considered as;

$$\gamma(x) = \gamma_0 x^b. \tag{S54}$$

Our EoS is comprised of five equations (Eqs. S50–S54), which require seven parameters (ρ_0, K_{T_0}, K'_{T_0}, γ_0, b, e_0, and g) in total. Using these equations, we can calculate the ρ and longitudinal wave velocity V_P of liquid iron for a given P-T (or P-ρ);

$$V_P = \sqrt{\frac{K_S}{\rho}}, \tag{S55}$$

where $K_S = K_T(1 + \alpha\gamma T)$ is adiabatic bulk modulus and $\alpha = -\left(\frac{1}{\rho}\right)\left(\frac{\partial\rho}{\partial T}\right)_P$ is thermal expansion coefficient.

Here we use; 1) the P–T–ρ data based on XRD data in this study up to 116 GPa, 2) the P–T–V_P data obtained from the present IXS measurements up to 45 GPa, and 3) the P–ρ–V_P–γ data from previous shock-wave experiments between 278 and 397 GPa (Table 2 in [8]). Based on these data, we have determined the seven EoS parameters so as to minimize the error-weighted sum of the squares of residuals between calculated and observed values. The obtained EoS parameters are as follows; ρ_0 = 7.03 g/cm^3, K_{T_0} = 82.1 GPa, K'_{T_0} =5.80, γ_0 = 2.02, b = 0.63, e_0 =0.68 × 10^{-4} K^{-1}, and g = −1.0 (T_0 = 1811 K). Fig. 4 shows that our EoS reproduces all of these experimental data well.

Although Nishida *et al.* [5] previously reported the V_P of liquid iron up to 5.8 GPa via ultrasonic method in a multi-anvil apparatus, we did not use their data here because of a possible structural change in liquid iron below 5 GPa near the δ–γ–liquid triple point [6]. Nevertheless, the present EoS reproduces their data (Fig. 4), indicating that the effect of such structural transformation is small, at least in terms of ρ and V_P. Note that our EoS is also consistent with the density at ambient pressure.

The isentropic temperature profile is given by the following thermodynamic relationships;

$$\left(\frac{\partial T}{\partial P}\right)_S = \frac{\alpha V T}{C_P} = \frac{\gamma_{\mathrm{th}} T}{K_S}, \tag{S56}$$

in which C_P represents isobaric heat capacity. Thus, an isentropic temperature profile referred to as geotherm is obtained by integrating Eq. S56 with the Grüneisen parameter γ for liquid iron determined in this study. We consider three different temperatures at the ICB; 5000 K, 5400 K (frequently used in the literature [3], and 5800 K, which correspond to 3710, 4000, and 4290 K, respectively, at the core-mantle boundary (CMB) (Fig. 4(c)). Then, density and velocity along these isentropic temperature profiles are calculated using the present EoS (Fig. 4(d, e) and Table SII).

The uncertainties in calculated density and velocity along the isentropic P–T path are evaluated on the basis of the Bayesian inference [48]. The results show that errors estimated from 68% and 95% credible intervals are within approximately ±0.8–1.2% and ±1.9–2.6%, respectively, for both density and velocity at the core pressure range, which are small enough to discuss the outer core composition based on the difference of liquid iron density and velocity from seismologically-deduced outer core density (PREM) [26].

Anderson and Ahrens (1994) [8] is one of the pioneering works on the EoS of liquid iron. They constructed the EoS of liquid iron from shock compression data together with data at ambient pressure. However, the shock experiments that they used in their EoS did not measure temperature. Therefore, their results, in particular for the thermal terms, largely depend on theoretical studies by the 1990's or earlier regarding the model of internal energy of liquid iron. Indeed, they overestimated the temperature by ~900 K at 278 GPa (Fig. S14). Recent theoretical studies [47,49] also suggested that the temperatures in Anderson and Ahrens (1994) [8] are overestimated. On the other hand, we measured temperatures by a spectro-radiometric method for all of our data points. Our EoS would serve an important reference for the property of liquid iron at high pressure.

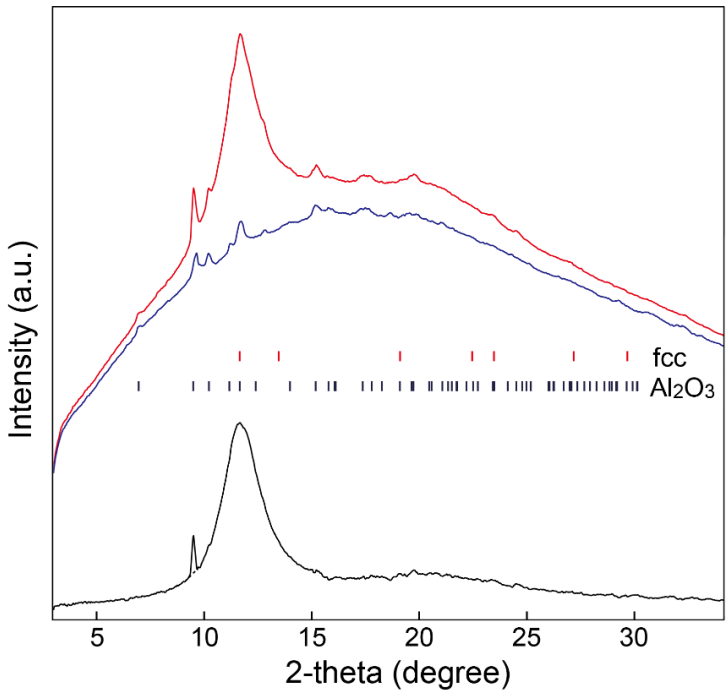

FIG. S1. X-ray diffraction spectra before (blue) and on (red) melting. Red and blue lines represent XRD spectra from liquid and solid (face-centered cubic, fcc) iron, collected at 2600 K and 2520 K at 21.5 GPa, respectively. The peak positions of fcc iron (red) and Al_2O_3 insulators (black) are indicated. The bottom spectrum (black) is the difference between the liquid and the solid, corresponding to a diffuse scattering signal from liquid iron. An intense peak at around 2-theta = 9.5° is the diffraction peak from the single crystal Al_2O_3 thermal insulator. Since the peak is very intense and exhibits blown-out highlights, it cannot be removed by subtracting background signals. This was removed considering a cubic spline for data processing (dashed line). The high frequency noises hardly effect on the final results on the calculated g(r) in the small r region (Fig. 1(b)).

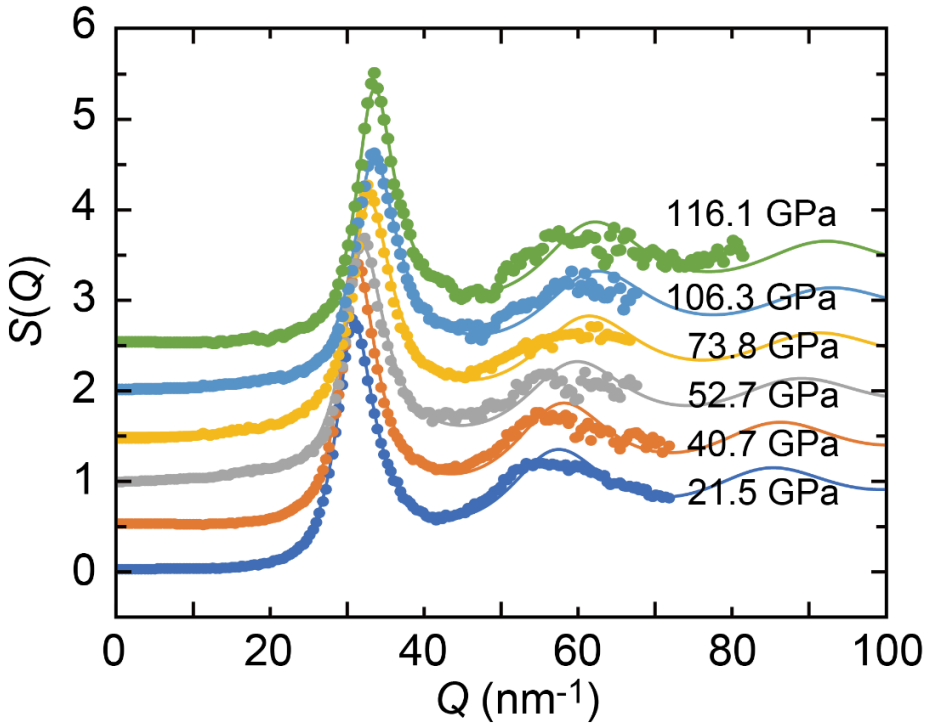

FIG. S2. Comparison of observed $S(Q)$ (dots) with fitting results assuming the hard sphere model (HSM), in which density is described only by two variables; the packing fraction and the hard sphere diameter [18] (solid lines). Although the first peaks at about 30~40 nm^{-1} can be well fitted to those of the HSM $S(Q)$ by adjusting the HSM variables, the second peaks of the experimental $S(Q)$ slightly shifts toward lower Q compared to the HSM $S(Q)$. Similar shifts of the second peaks were also reported in a previous study on liquid aluminum [4].

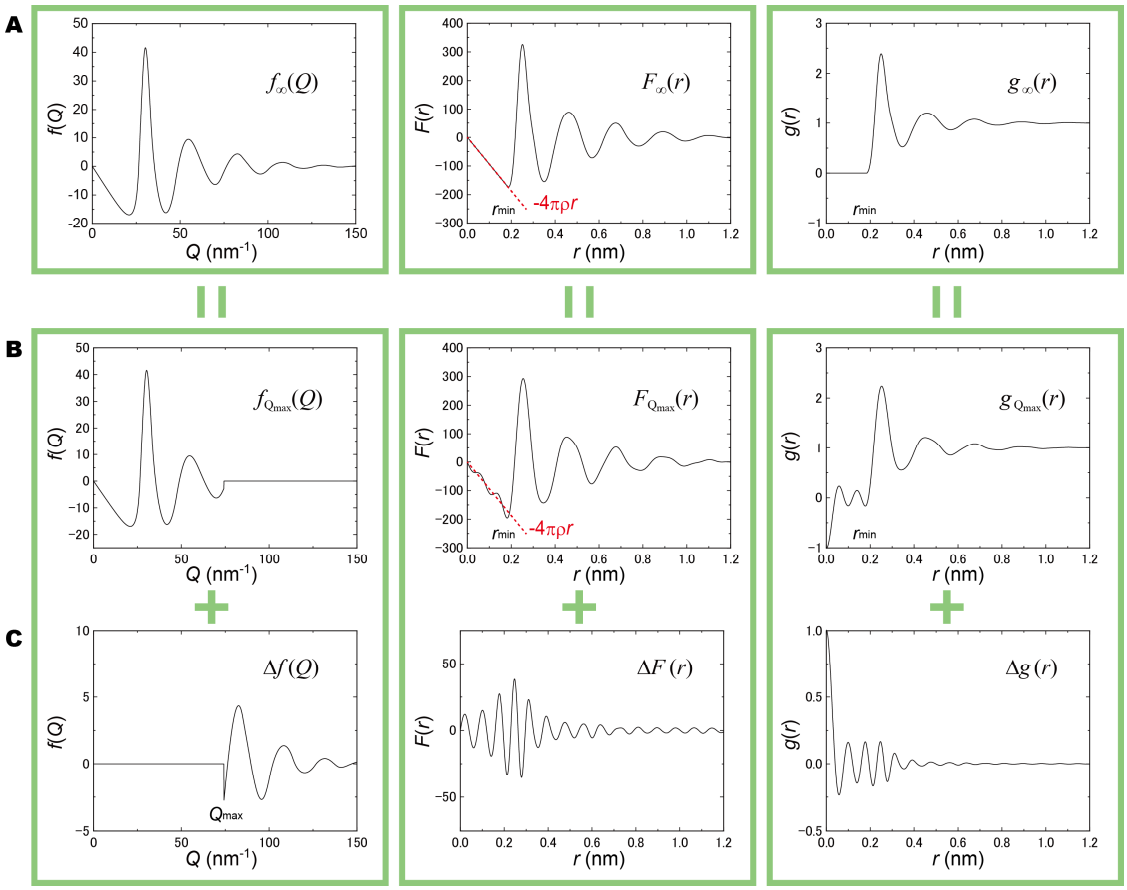

FIG. S3. $f_{\infty}(Q)$, $f_{Q\max}(Q)$, and $\Delta f(Q)$ and their corresponding $F(r)$ and $g(r)$. (A) An example of true $f_{\infty}(Q)$, $F_{\infty}(r)$, and $g_{\infty}(r)$. $F_{\infty}(r)$ should be $-4\pi\rho r$ (red dashed line) at $r \leq r_{\min}$ because $g_{\infty}(r) = 0$ (no atom exists within the distance between the nearest neighbor atoms, $r_{\min}$). In order to prepare true $f_{\infty}(Q)$, we start with distribution function $F(r)$ for a non-crystalline material, considering that $F(r)$ is a linear function of r at $r < 0.18$ nm, the average inter-atomic distance is about 0.25 nm, and $F(r)$ approaches 0 at $r \rightarrow$ infinity. Then, it was transformed to $f_{\infty}(Q)$. (B) $f_{Q\max}(Q)$ that is truncated at a finite $Q_{\max}$ ($< \infty$) (Eq. S10), and $F_{Q\max}(r)$ and $g_{Q\max}(r)$ calculated from $f_{Q\max}(Q)$ (Eqs. S11, S12). (C) $\Delta f(Q)$, $\Delta F(r)$, and $\Delta g(r)$ (Eqs. S13–S15). Note that $f_{\infty}(Q) = f_{Q\max}(Q) + \Delta f(Q)$, $F_{\infty}(r) = F_{Q\max}(r) + \Delta F(r)$, and $g_{\infty}(r) = g_{Q\max}(r) + \Delta g(r)$. See section 2 for more details.

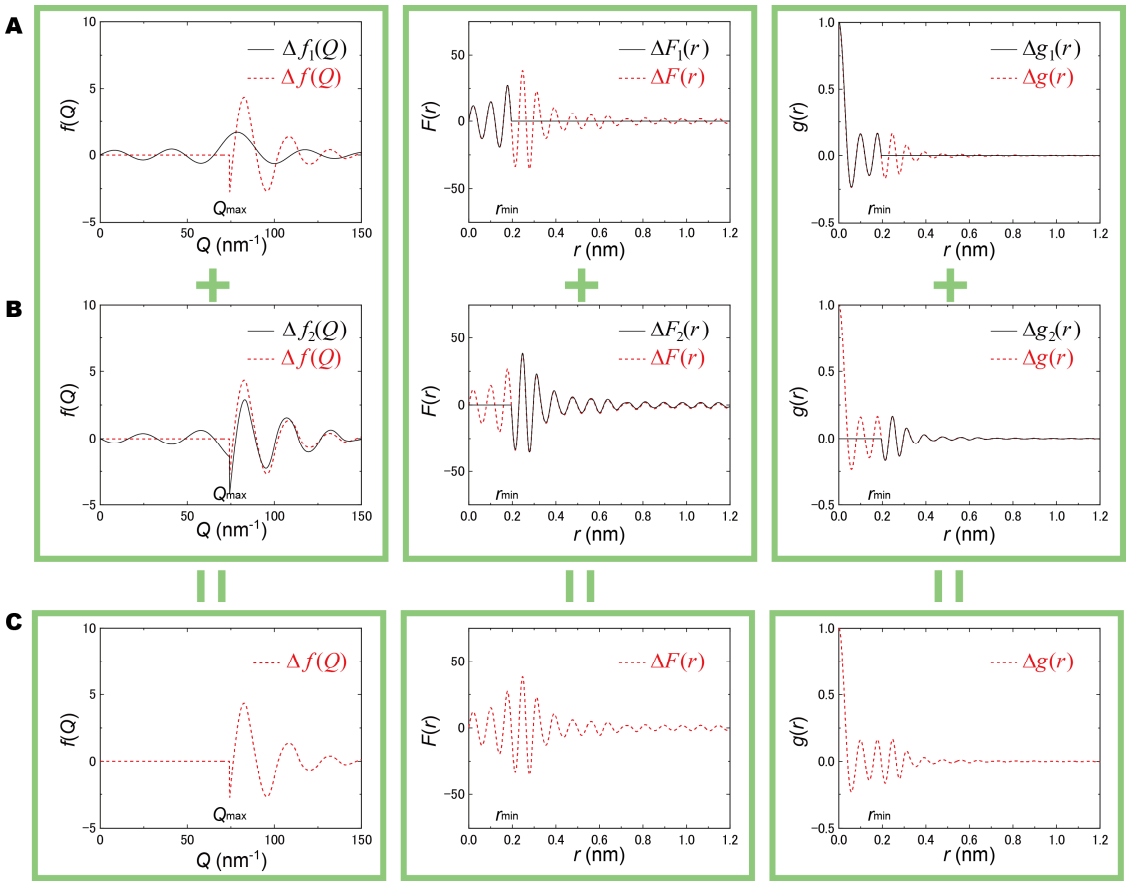

FIG. S4. $\Delta f_1(Q)$, $\Delta f_2(Q)$, and $\Delta f(Q)$ and their corresponding $\Delta F(r)$ and $\Delta g(r)$. (A) $\Delta f_1(Q)$, $\Delta F_1(r)$, and $\Delta g_1(r)$. (B) $\Delta f_2(Q)$, $\Delta F_2(r)$, and $\Delta g_2(r)$. (C) $\Delta f(Q)$, $\Delta F(r)$, and $\Delta g(r)$. Red dashed lines in (A) and (B) are $\Delta f(Q)$, $\Delta F(r)$, and $\Delta g(r)$ for comparison.

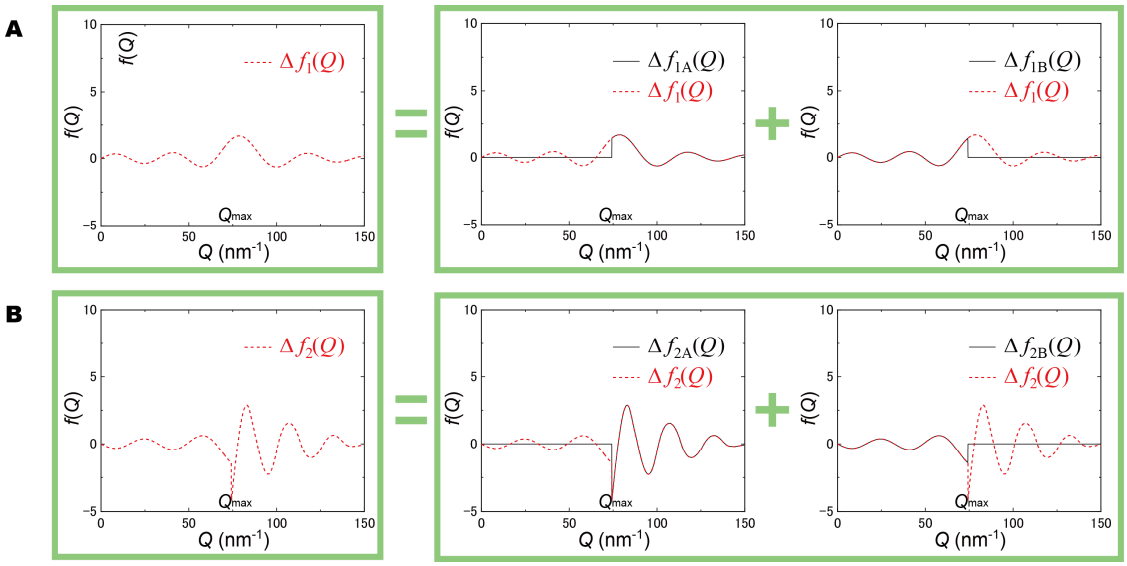

FIG. S5. $\Delta f_1(Q)$, $\Delta f_{1A}(Q)$, $\Delta f_{1B}(Q)$, $\Delta f_2(Q)$, $\Delta f_{2A}(Q)$, and $\Delta f_{2B}(Q)$ in Eqs. S27–S30. (A) $\Delta f_1(Q)$, $\Delta f_{1A}(Q)$, and $\Delta f_{1B}(Q)$. (B) $\Delta f_2(Q)$, $\Delta f_{2A}(Q)$, and $\Delta f_{2B}(Q)$.

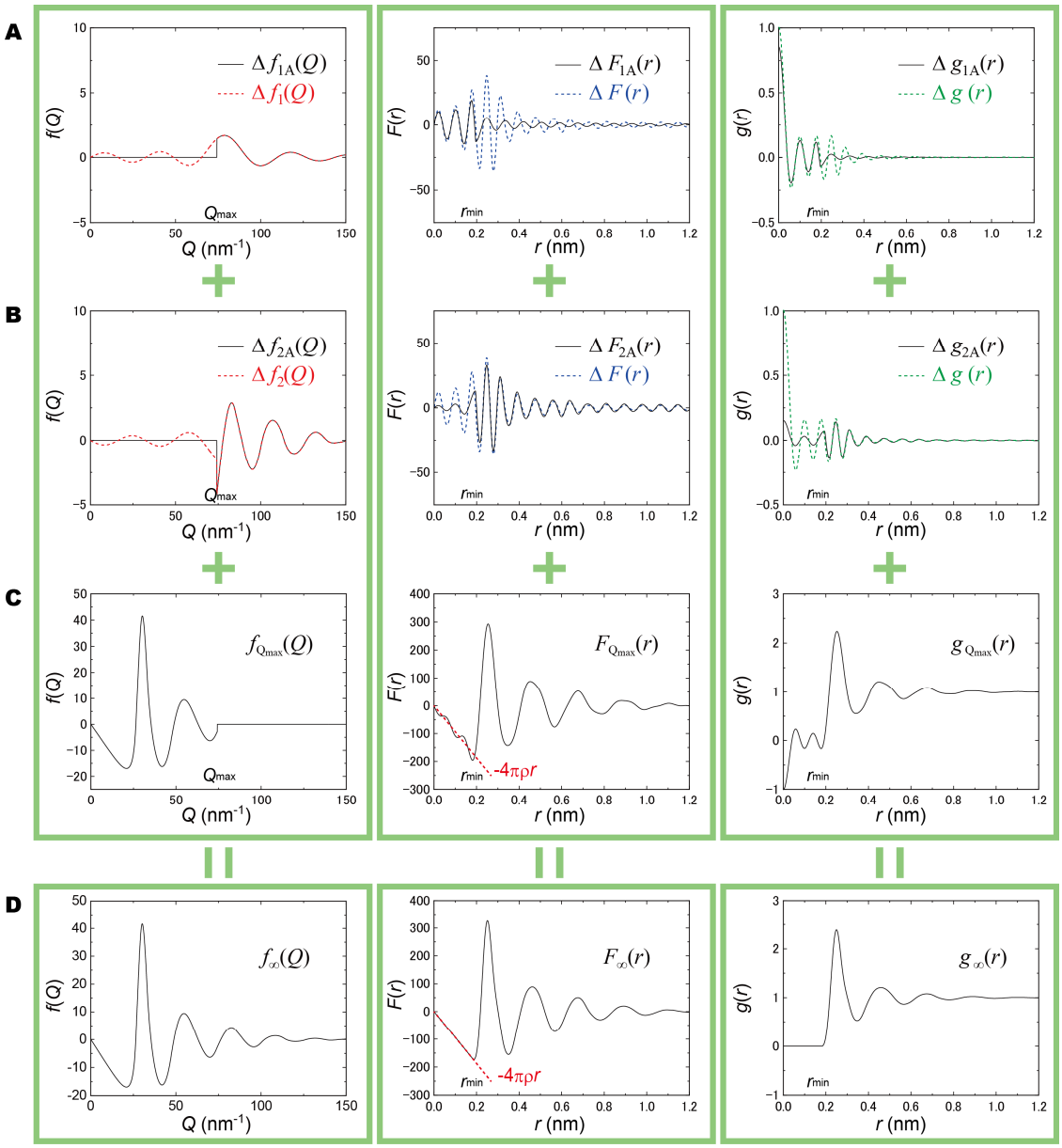

FIG. S6. $\Delta f_{1A}(Q)$, $\Delta f_{2A}(Q)$, $f_{Q\max}(Q)$, and $f_{\infty}(Q)$ and their corresponding $\Delta F(r)$ and $\Delta g(r)$. (A) $\Delta f_{1A}(Q)$, $\Delta F_{1A}(r)$, and $\Delta g_{1B}(r)$. (B) $\Delta f_{2A}(Q)$, $\Delta F_{2A}(r)$ and $\Delta g_{2B}(r)$. (C) $f_{Q\max}(Q)$, $F_{Q\max}(r)$ and $g_{Q\max}(r)$. (D) $f_{\infty}(Q)$, $F_{\infty}(r)$ and $g_{\infty}(r)$. $\Delta F(r)$ (blue dashed line) and $\Delta g(r)$ (green dashed line) are also shown for comparison in A and B.

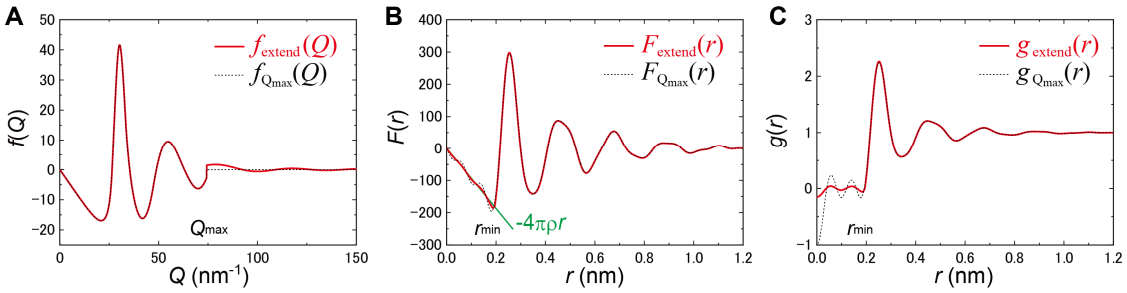

FIG. S7. Comparison of extended $f_{extend}(Q)$ with truncated $f_{Qmax}(Q)$ and their corresponding $F(r)$ and $g(r)$. (A) Extended $f_{extend}(Q)$. (B, C) Calculated $F_{extend}(r)$ and $g_{extend}(r)$ from $f_{extend}(Q)$.

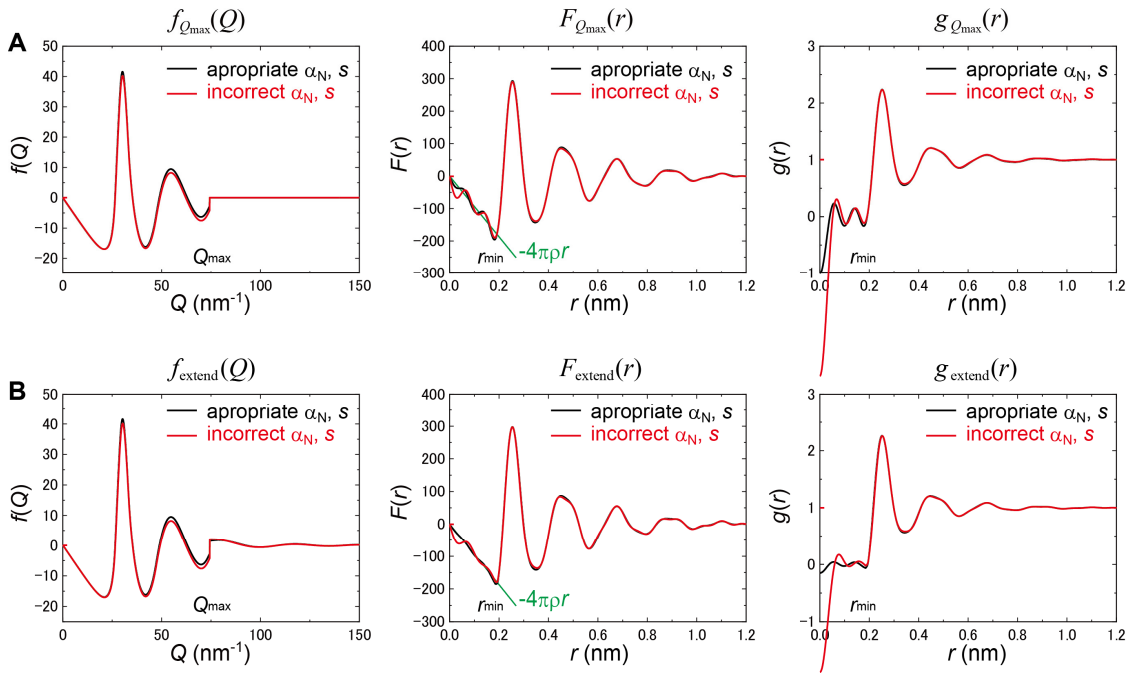

FIG. S8. Effect of errors in α_N and s on $F(r)$ and $g(r)$. (A) Calculated $f_{Q\max}(Q)$ from appropriate/incorrect (black/red) α_N and s, and corresponding $F_{Q\max}(r)$ and $g_{Q\max}(r)$. (B) Extended $f_{\mathrm{extend}}(Q)$ and corresponding $F_{\mathrm{extend}}(r)$ and $g_{\mathrm{extend}}(r)$. If α_N and s used to obtain $f_{Q\max}(Q)$ include errors (red lines), any extended $f(Q)$ at $Q > Q_{\max}$ does not reduce oscillations in $F(r)$ and $g(r)$ at $r \leq r_{\min}$.

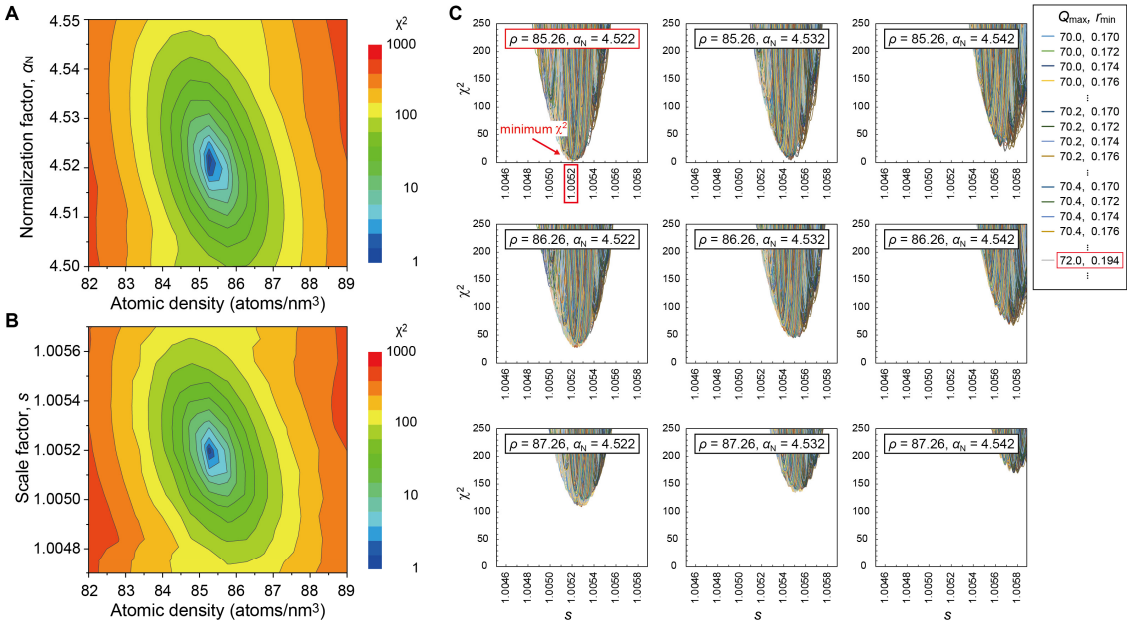

FIG. S9. Contour plots of the figure of merit χ^2 (Eq. S43) for run #1. (A) Normalization factor α_N–atomic density ρ plane and (B) scale factor s–atomic density ρ plane. The unique minimum at ρ = 85.26 atoms/nm^3 gives us the density for the studied liquid. χ^2 is normalized to 1 at the minimum. Color represents the minimum χ^2 for each pair of ρ and α_N (or s), which are obtained by searching the best parameter set of Q_{max}, r_{min}, and s (or α_N). (C) A part of the calculation result used for A and B. Lines represent figure of merit χ^2 as a function of s for a certain set of ρ, α_N, Q_{max} and r_{min}. For each pair of ρ and α_N, χ^2 is calculated with changing the other parameters (Q_{max}, r_{min}, and s). There is a unique set of parameters (s = 1.0052, α_N = 4.522, r_{min} = 0.194 nm, and Q_{max} = 72.0 nm^{-1}, giving ρ = 85.26 atoms/nm^3 (7.91 g/cm^3)), which minimize χ^2 in the ranges of 1±0.5 for s, ±50% from the value obtained by the Krogh-Moe and Norman's method [15] for α_N, ±50% from the density of solid iron at the P-T condition of an experiment for ρ, and 0.15 to 0.30 nm for r_{min} (0.30 nm is larger than the first peak position in $g(r)$).

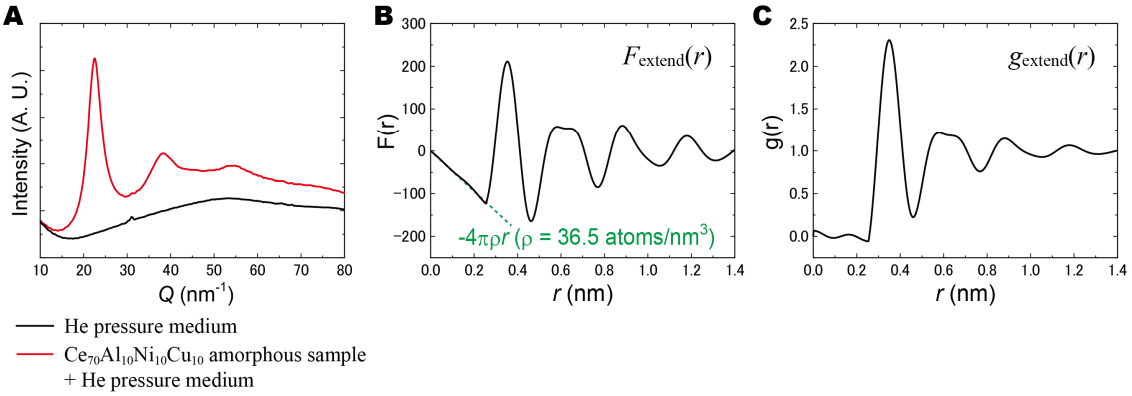

FIG. S10. (A) XRD patterns collected between 0.2 and 0.5 GPa for a Ce-based metallic glass ($Ce_{70}Al_{10}Ni_{10}Cu_{10}$) in a He pressure medium (red) and for the He pressure medium only (black) in a DAC [42]. (B and C) $F_{extend}(r)$ and $g_{extend}(r)$ obtained by the present new analytical method. We obtained the atomic density of 36.5 ± 0.2 atoms/nm^3, consistent with the known density.

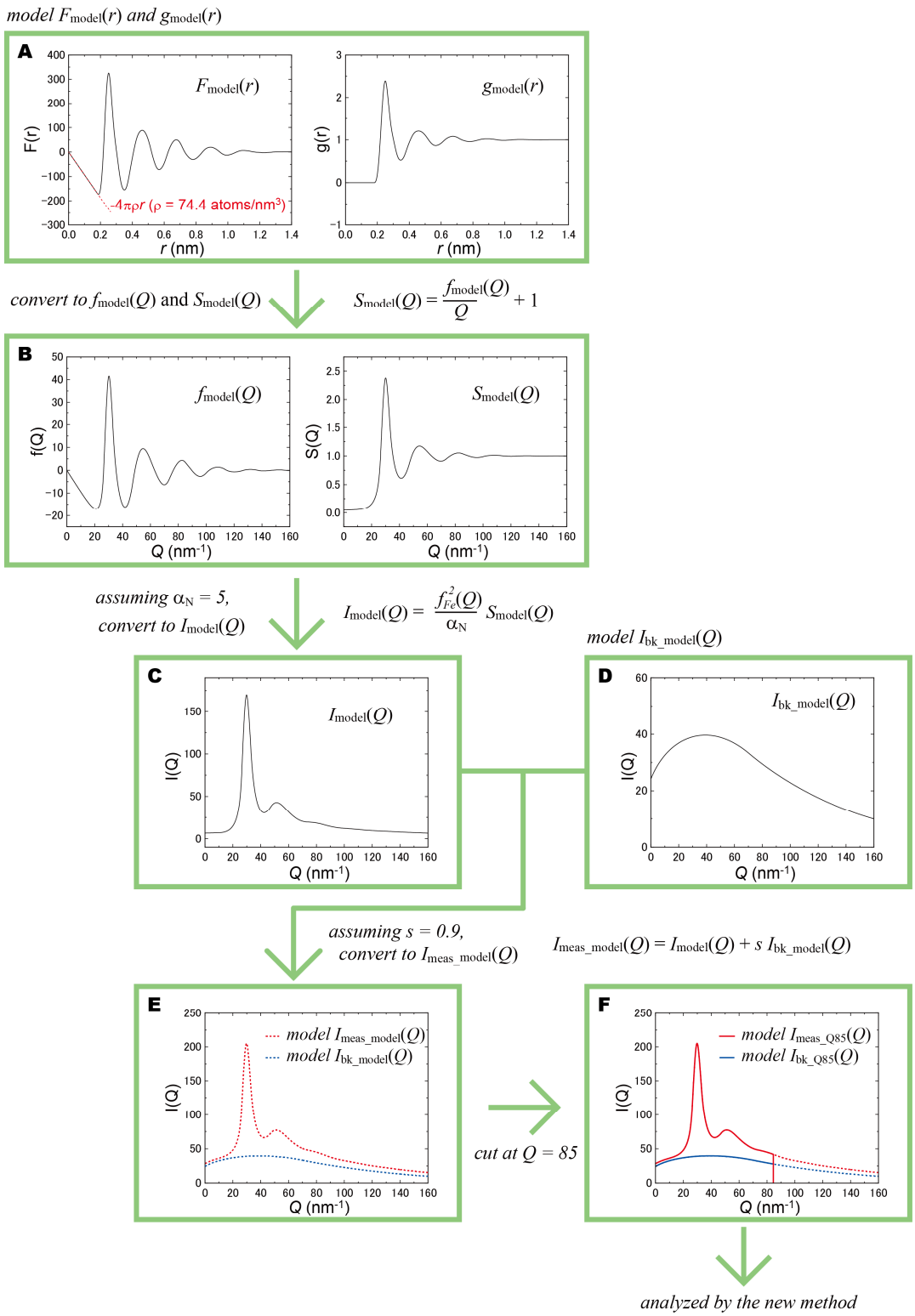

FIG. S11. (A) Synthetic model $F_{model}(r)$ and $g_{model}(r)$ for an atomic density ρ = 74.4 atoms/nm^3. (B–E) Synthetic XRD signal $I_{meas\_model}(Q)$ and $I_{bk\_model}(Q)$ prepared from $F_{model}(r)$ and $g_{model}(r)$. (F) $I_{meas\_model}(Q)$ and $I_{bk\_model}(Q)$ terminated at Q = 85 nm^{-1} ($I_{meas\_Q85}(Q)$ and $I_{bk\_Q85}(Q)$).

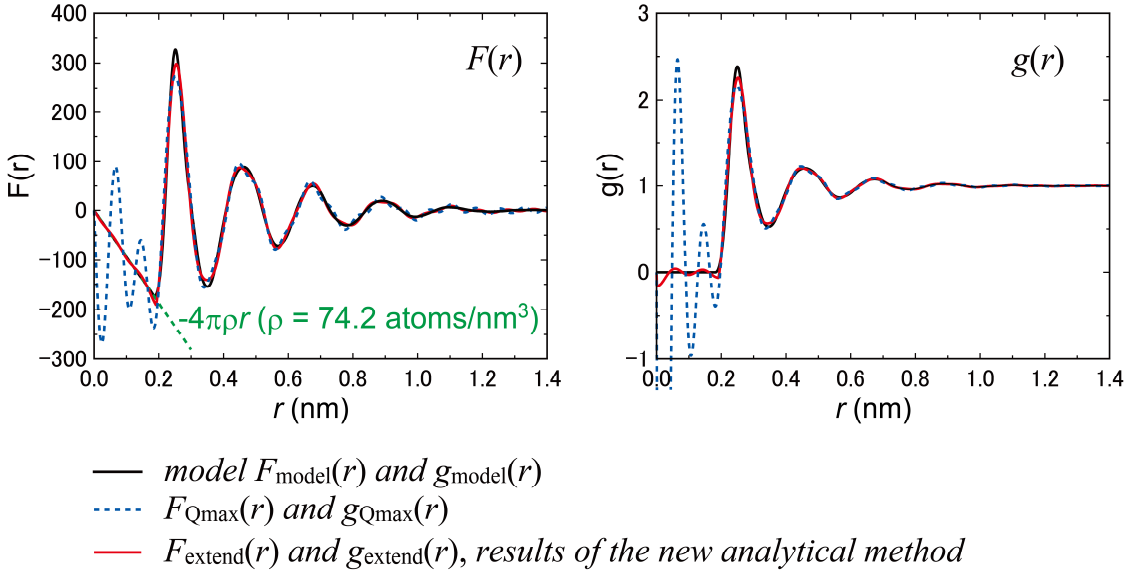

FIG. S12. Black lines, $F_{\mathrm{model}}(r)$ and $g_{\mathrm{model}}(r)$ (same with Fig. S11A). Blue dashed lines, $F_{\mathrm{Qmax}}(r)$ and $g_{\mathrm{Qmax}}(r)$. Red lines, $F_{\mathrm{extend}}(r)$ and $g_{\mathrm{extend}}(r)$ obtained by the new method.

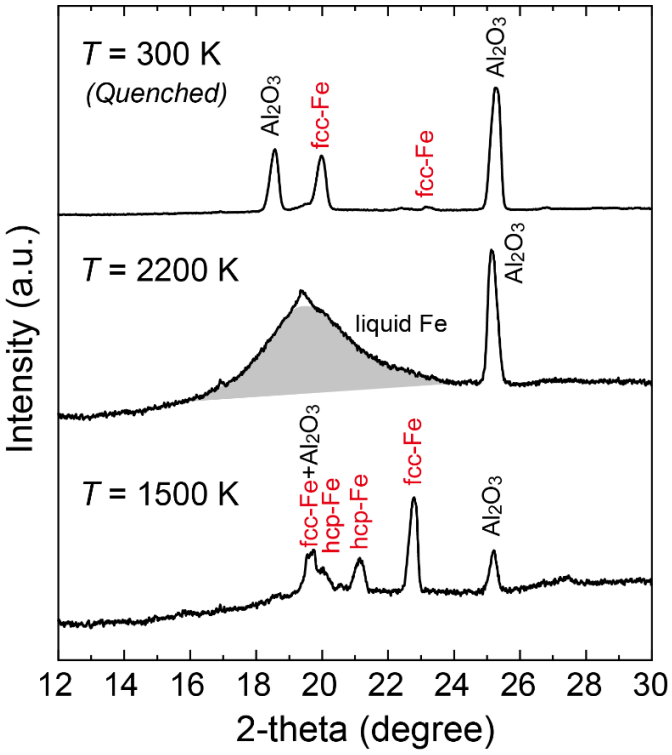

FIG. S13. X-ray diffraction spectra before and after IXS measurements at 16 GPa (run #12). They were collected at 1500 K (bottom) and 2200 K (middle) during heating, and at 300 K after heating (top). All peaks from the solid sample disappeared and the diffuse scattering signal from liquid (gray) was observed at 2200 K, indicating the sample was molten. The wavelength of an incident x-ray was 0.6968 Å. The peaks labeled with Al_2O_3 were from a thermal insulator of sapphire.

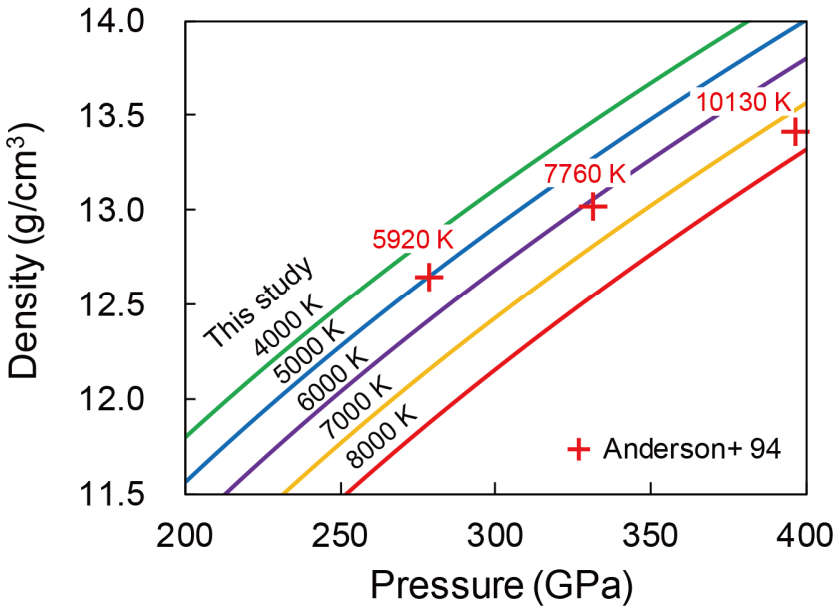

FIG. S14. Isothermal P–ρ relations calculated from our EoS for 4000 K (green), 5000 K (blue), 6000 K (purple), 7000 K (yellow), and 8000 K (red). Red crosses are shock-compression data with temperatures (red numbers) estimated in Anderson and Ahrens [8].

Table SI. Lattice parameters and volumes of fcc Fe, hcp Fe, and KCl used for pressure determination.

			fcc Fe		hcp Fe			KCl	
run no.	P (GPa)	T (K)	V (Å^3)	a (Å)	V (Å^3)	a (Å)	c (Å)	V (Å^3)	a (Å)
#1	21.5	2460	45.16	3.561				33.95	3.238
#2	31.3	2870							
#3	40.6	2840	41.97	3.475					
#4	40.7	2860	41.99	3.476					
#5	52.7	3080	40.49	3.434					
#6	52.8	3050	40.44	3.432					
#7	68.5	3310	38.84	3.387					
#8	69.8	3340	38.73	3.383					
#9	73.8	3630						27.66	3.024
#10	106.3	4220			17.82	2.337	3.766		
#11	116.1	4340			17.52	2.318	3.764		
#12	16.0	2200	46.04	3.584					
#13	32.7	2700	43.16	3.508					
#14	44.9	2700	41.08	3.450					

Table SII. Isothermal P–ρ and P–V_P relations of liquid iron.

	ρ (g/cm^3)				V_P (km/s)			
P (GPa)	2000 K	3000 K	4000 K	5000 K	2000 K	3000 K	4000 K	5000 K
0	6.90				3.93			
5	7.30				4.30	4.16		
10	7.63	7.03			4.59	4.50	4.44	
15	7.91	7.39			4.85	4.78	4.75	
20	8.15	7.69	7.08		5.07	5.02	5.00	5.06
25	8.37	7.95	7.41		5.27	5.23	5.23	5.28
30	8.57	8.18	7.69	7.06	5.45	5.42	5.43	5.48
35	8.75	8.39	7.94	7.37	5.62	5.60	5.61	5.66
40	8.93	8.58	8.16	7.64	5.78	5.76	5.78	5.83
45	9.09	8.76	8.36	7.88	5.92	5.91	5.93	5.99
50	9.25	8.93	8.55	8.10	6.06	6.06	6.08	6.13
55	9.39	9.09	8.73	8.30	6.19	6.19	6.21	6.27
60	9.53	9.24	8.89	8.48	6.32	6.32	6.34	6.40
65	9.67	9.38	9.05	8.66	6.44	6.44	6.47	6.52
70	9.80	9.52	9.20	8.82	6.55	6.55	6.58	6.64
75	9.92	9.65	9.34	8.98	6.66	6.66	6.69	6.75
80	10.04	9.78	9.48	9.13	6.76	6.77	6.80	6.86
85	10.16	9.90	9.61	9.27	6.86	6.87	6.90	6.96
90	10.27	10.02	9.73	9.40	6.96	6.97	7.00	7.06
95	10.38	10.14	9.86	9.53	7.05	7.07	7.10	7.16
100	10.48	10.25	9.97	9.66	7.15	7.16	7.19	7.25
110	10.69	10.46	10.20	9.89	7.32	7.33	7.37	7.43
120	10.88	10.66	10.41	10.12	7.48	7.50	7.53	7.60
130	11.06	10.85	10.61	10.33	7.64	7.65	7.69	7.75
140	11.24	11.04	10.80	10.53	7.79	7.80	7.84	7.90
150	11.41	11.21	10.98	10.72	7.93	7.94	7.98	8.04
160	11.57	11.38	11.16	10.90	8.06	8.08	8.12	8.18
170	11.73	11.54	11.32	11.07	8.19	8.21	8.25	8.31
180	11.88	11.70	11.49	11.24	8.31	8.33	8.37	8.44

Table SII. (contiuned)

	ρ (g/cm^3)				V_P (km/s)			
P (GPa)	2000 K	3000 K	4000 K	5000 K	2000 K	3000 K	4000 K	5000 K
190	12.03	11.85	11.64	11.40	8.43	8.46	8.50	8.56
200	12.18	12.00	11.79	11.56	8.55	8.57	8.61	8.67
210	12.32	12.14	11.94	11.71	8.66	8.68	8.72	8.78
220	12.45	12.28	12.09	11.86	8.77	8.79	8.83	8.89
230	12.59	12.42	12.22	12.00	8.88	8.90	8.94	9.00
240	12.72	12.55	12.36	12.14	8.98	9.00	9.04	9.10
250	12.84	12.68	12.49	12.28	9.08	9.10	9.14	9.20
260	12.97	12.81	12.62	12.41	9.17	9.20	9.24	9.29
270	13.09	12.93	12.75	12.54	9.27	9.29	9.33	9.39
280	13.21	13.05	12.87	12.66	9.36	9.38	9.42	9.48
290	13.32	13.17	12.99	12.79	9.45	9.47	9.51	9.57
300	13.44	13.29	13.11	12.91	9.53	9.56	9.60	9.66
310	13.55	13.40	13.23	13.03	9.62	9.64	9.68	9.74
320	13.66	13.51	13.34	13.14	9.70	9.72	9.77	9.82
330	13.77	13.62	13.45	13.26	9.78	9.81	9.85	9.90
340	13.87	13.73	13.56	13.37	9.86	9.89	9.93	9.98
350	13.98	13.84	13.67	13.48	9.94	9.96	10.00	10.06
360	14.08	13.94	13.77	13.59	10.01	10.04	10.08	10.14
370	14.18	14.04	13.88	13.69	10.09	10.11	10.15	10.21

Table SIII. P–T–ρ–V_P relations of liquid iron along isentropic temperature profiles with T_{ICB} = 5800, 5400, and 5000 K.

	T_{ICB} = 5800 K			T_{ICB} = 5400 K			T_{ICB} = 5000 K			PREM†		
P (GPa)	T (K)	ρ (g/cm^3)	V_P (km/s)	T (K)	ρ (g/cm^3)	V_P (km/s)	T (K)	ρ (g/cm^3)	V_P (km/s)	P (GPa)	ρ (g/cm^3)	V_P (km/s)
135.75	4293	10.64	7.79	4005	10.72	7.78	3715	10.79	7.76	135.75	9.903	8.065
144.19	4379	10.78	7.92	4084	10.85	7.91	3788	10.93	7.89	144.19	10.029	8.199
165.12	4581	11.10	8.22	4271	11.18	8.20	3960	11.25	8.18	165.12	10.327	8.513
185.64	4765	11.39	8.49	4441	11.47	8.47	4117	11.55	8.45	185.64	10.602	8.796
205.60	4933	11.66	8.73	4597	11.74	8.71	4260	11.82	8.69	205.60	10.853	9.050
224.85	5086	11.91	8.95	4738	11.99	8.93	4390	12.07	8.90	224.85	11.083	9.279
243.25	5225	12.13	9.15	4867	12.22	9.12	4509	12.30	9.10	243.25	11.293	9.484
260.68	5351	12.34	9.33	4984	12.42	9.30	4617	12.50	9.28	260.68	11.483	9.669
277.04	5465	12.52	9.49	5090	12.61	9.46	4714	12.69	9.43	277.04	11.655	9.835
292.22	5567	12.69	9.63	5184	12.77	9.60	4801	12.86	9.58	292.22	11.809	9.986
306.15	5658	12.84	9.76	5268	12.92	9.73	4878	13.01	9.70	306.15	11.947	10.123
318.75	5737	12.97	9.87	5342	13.06	9.84	4947	13.14	9.81	318.75	12.069	10.250
328.85	5800	13.07	9.95	5400	13.16	9.92	5000	13.24	9.89	328.85	12.166	10.356

†The preliminary reference Earth model (PREM) [26] for comparison.